INTERNATIONAL JOURNAL FOR NUMERICAL AND ANALYTICAL METHODS IN GEOMECHANICS
Int. J. Numer. Anal. Meth. Geomech. 2008; **32**:1023–1050
Published online 6 September 2007 in Wiley InterScience (www.interscience.wiley.com). DOI: 10.1002/nag.657

Arbitrary Lagrangian–Eulerian method for large-strain consolidation problems

Majidreza Nazem*,†, Daichao Sheng, John P. Carter and Scott W. Sloan

Centre for Geotechnical and Materials Modelling, School of Engineering, The University of Newcastle, Newcastle, NSW, Australia

SUMMARY

In this paper, an arbitrary Lagrangian–Eulerian (ALE) method is generalized to solve consolidation problems involving large deformation. Special issues such as pore-water pressure convection, permeability and void ratio updates due to rotation and convection, mesh refinement and equilibrium checks are discussed. A simple and effective mesh refinement scheme is presented for the ALE method. The ALE method as well as an updated-Lagrangian method is then used to solve some classical consolidation problems involving large deformations with different constitutive laws. The results clearly show the advantage and efficiency of the ALE method for these examples. Copyright © 2007 John Wiley & Sons, Ltd.

Received 18 January 2006; Revised 13 July 2007; Accepted 13 July 2007

KEY WORDS: consolidation; ALE method; mesh motion; time stepping; stress integration

1. INTRODUCTION

In geotechnical problems, deformation is usually coupled with the flow of pore fluids. A coupled finite element procedure combines the equilibrium equation and the continuity equation through the effective stress principle and the volumetric strain rate. On the basis of the theory of consolidation of Biot [1], several large deformation formulations for coupled problems can be found in the literature. Carter *et al.* [2] presented a general theory of elastic finite-strain consolidation which was later generalized to elastoplastic consolidation [3]. Prevost [4, 5] derived a generalized incremental form of Biot's consolidation involving finite strains and material nonlinearity. Large deformation in saturated and unsaturated porous media under dynamic loads was studied, respectively, by Zienkiewicz and Shiomi [6] and Meroi *et al.* [7]. In all these studies, constitutive equations expressed in the rate form are normally used to integrate for the stresses over calculated strain increments.

*Correspondence to: Majidreza Nazem, Centre for Geotechnical and Materials Modelling, School of Engineering, The University of Newcastle, Newcastle, NSW 2308, Australia.
†E-mail: majidreza.nazem@newcastle.edu.au

On the basis of multiplicative decomposition of deformation gradients (e.g. see [8–10], Borja and Alarcon [11]) presented a mathematical formulation for elastoplastic finite-strain consolidation, which has been implemented using the finite element method by Borja *et al*. [12]. Following the same approach using multiplicative decomposition of deformation gradients, Sanavia *et al*. [13] presented a large strain formulation for saturated and partially saturated porous media. This type of formulation circumvents the rate-type stress integration in large deformation analysis and can also handle large elastic strains. To handle both the rate-type and the multiplicative decomposition formulations, an updated-Lagrangian (UL) method is usually adopted where the coordinates of material points are updated according to the displacements after each time increment. In the case of relatively large deformations, the UL method can lead to severe mesh distortion that can cause spontaneous termination of the analysis.

The arbitrary Lagrangian–Eulerian (ALE) method, on the other hand, was developed to handle large deformation problems with severe mesh distortion in solid mechanics and fluid mechanics. This method, however, has not attracted much attention in geomechanics—mainly due to its complexity, particularly in coupled problems involving both deformation and flow of pore fluids. A recent study by Nazem *et al.* [14] showed that the ALE method, based on the operator-split technique [15], can provide an effective solution to the mesh distortion problem encountered in the UL method.

This paper presents an ALE formulation for consolidation problems. The ALE method is based on the operator-split technique where a Lagrangian solution is convected to an Eulerian mesh. The Lagrangian solution, which by itself is also a complete solution of the problem and is referred to as the UL method, is presented first. Particular attention is then paid to the mesh motion scheme and the convection of pore-water pressure and state variables in the Eulerian step. The numerical performance of the UL and the ALE methods is then compared through several numerical examples of consolidation problems.

2. LAGRANGIAN FORMULATION

2.1. Governing equations

In the UL method, the equilibrium equation states [16]

$$\nabla^{\mathrm{T}} \sigma_{ij}^{t+\Delta t} + b_i^{t+\Delta t} = 0 \tag{1}$$

where σ_{ij} denotes the true (Cauchy) stress tensor, b_i is the body force vector and ∇ represents the gradient operator. The right superscript denotes the time when the quantities are measured. The basic assumption in Equation (1) is that all the variables and state parameters are known up to time t and the aim is to find the unknowns at time $t + \Delta t$. The principle of effective stress relates the total Cauchy stresses to the effective Cauchy stress, σ'_{ij}, through the pore-water pressure, p,

$$\mathrm{d}\sigma_{ij} = \mathrm{d}\sigma'_{ij} + \mathrm{d}p \cdot \delta_{ij} \tag{2}$$

where δ_{ij} is the Kronecker-delta. In a large deformation analysis, the effect of rigid body rotations must be considered in the stress–strain relations. This is often taken into account by a frame-independent stress rate. In this study the Jaumann stress rate is used, which is defined as

$$\mathrm{d}\widetilde{\sigma}'_{ij} = \mathrm{d}\sigma'_{ij} - \sigma'_{ik}\mathrm{d}\Omega_{kj} - \sigma'_{jk}\mathrm{d}\Omega_{ki} = C'_{ijkl} \cdot \mathrm{d}\varepsilon_{kl} \tag{3}$$

DOI: 10.1002/nag

where Ω is the spin tensor, C' is the material constitutive matrix and ε_{ij} is the linear strain tensor. Note that in Equation (3), the Jaumann stress rate is only applied to the effective stress since the pore-water pressure is frame independent and its unique component does not change under rigid body rotation. Introducing Equations (2) and (3) into the equilibrium equation and applying the standard finite element procedure, the following matrix rate equation representing the equilibrium of the body can be obtained:

$$\dot{\mathbf{F}}^{\text{int}} = \mathbf{K}^{\text{ep}}\dot{\mathbf{U}} + \mathbf{L}\dot{\mathbf{P}} = \dot{\mathbf{F}}^{\text{ext}} \tag{4}$$

where $\mathbf{K}^{\text{ep}}$ and $\mathbf{L}$ are the stiffness and coupling matrices, respectively, $\mathbf{F}^{\text{ext}}$ is the external force vector and $\mathbf{F}^{\text{int}}$ represents the internal force vector. Detailed expressions for $\mathbf{K}^{\text{ep}}$, $\mathbf{L}$ and $\mathbf{F}^{\text{int}}$ can be found in the Appendix.

Denoting v_{s} as the velocity of soil particles and $\widetilde{v}$ as the superficial velocity of the fluid relative to the soil skeleton, we can write the conservation of mass as

$$\frac{\partial v_{\text{s}i}}{\partial x_i} + \frac{\partial \widetilde{v}_i}{\partial x_i} = 0 \tag{5}$$

In deriving Equation (5) it is assumed that the soil solids and the pore water are much less compressible than the soil skeleton. Darcy's Law states that the superficial velocity of the fluid relative to the soil skeleton is proportional to the hydraulic gradient

$$\widetilde{v}_i = n(v_{\text{w}i} - v_{\text{s}i}) = -\frac{k_{ij}}{\gamma_{\text{w}}}\left(\frac{\partial p}{\partial x_j} - b_{\text{w}j}\right) \tag{6}$$

where n is the porosity of soil, v_{w} is the velocity of pore fluid, k represents the permeability tensor, $b_{\text{w}} = \{0, \gamma_{\text{w}}, 0\}^{\text{T}}$ and γ_{w} is the unit weight of the fluid.[‡] Combining Darcy's law with the conservation of mass and following standard finite element linearisation, the following equation can be obtained (e.g. see [17])

$$\mathbf{L}^{\text{T}}\dot{\mathbf{U}} + \dot{\mathbf{H}}\mathbf{P} = \dot{\mathbf{Q}}^{\text{ext}} \tag{7}$$

where $\mathbf{H}$ is the flow matrix and $\mathbf{Q}$ is the fluid supply vector. Details of the matrices and vectors in the equation above are given in the Appendix.

2.2. Time stepping

Equations (4) and (7) form the global system of equations as

$$\begin{bmatrix} \mathbf{K}^{\text{ep}} & \mathbf{L} \\ \mathbf{L}^{\text{T}} & \mathbf{0} \end{bmatrix} \begin{Bmatrix} \dot{\mathbf{U}} \\ \dot{\mathbf{P}} \end{Bmatrix} + \begin{bmatrix} \mathbf{0} & \mathbf{0} \\ \mathbf{0} & \dot{\mathbf{H}} \end{bmatrix} \begin{Bmatrix} \mathbf{U} \\ \mathbf{P} \end{Bmatrix} = \begin{Bmatrix} \dot{\mathbf{F}}^{\text{ext}} \\ \dot{\mathbf{Q}}^{\text{ext}} \end{Bmatrix} \tag{8}$$

Equation (8) is usually written in the compact form as

$$\mathbf{C}\dot{\mathbf{X}} + \mathbf{K}\mathbf{X} = \dot{\mathbf{W}}^{\text{ext}} \tag{9}$$

[‡]The expression for b_{w} assumes that gravity acts in the negative 2-coordinate (y) direction.

DOI: 10.1002/nag

with

$$\mathbf{C}=\begin{bmatrix}\mathbf{K}^{\mathrm{ep}} & \mathbf{L}\\ \mathbf{L}^{\mathrm{T}} & \mathbf{0}\end{bmatrix},\quad \mathbf{K}=\begin{bmatrix}\mathbf{0} & \mathbf{0}\\ \mathbf{0} & \dot{\mathbf{H}}\end{bmatrix},\quad \mathbf{X}=\begin{Bmatrix}\mathbf{U}\\ \mathbf{P}\end{Bmatrix},\quad \dot{\mathbf{X}}=\begin{Bmatrix}\dot{\mathbf{U}}\\ \dot{\mathbf{P}}\end{Bmatrix},\quad \dot{\mathbf{W}}^{\mathrm{ext}}=\begin{Bmatrix}\dot{\mathbf{F}}^{\mathrm{ext}}\\ \dot{\mathbf{Q}}^{\mathrm{ext}}\end{Bmatrix}$$

Various time-stepping schemes exist in the literature for solving Equation (9), e.g. Booker and Small [18], Wood [19], Lewis and Schrefler [20] and Sloan and Abbo [21]. In this study, the commonly used θ-method is used to avoid further complications. Choosing $\theta=1$ leads to a classical backward Euler scheme shown as

$$\mathbf{C}\{\mathbf{X}_{n+1}-\mathbf{X}_n\}+h\mathbf{K}\mathbf{X}_{n+1}=h\dot{\mathbf{W}}^{\mathrm{ext}}_{n+1} \tag{10}$$

In the case of constants **C** and **K**, such as in small deformation analysis of elastic soil with constant permeability, the system of equations defined by (10) can be solved for $\mathbf{X}_{n+1}$. In more general cases, **C** and **K** depend on **X** and are evaluated at $\mathbf{X}_{n+1}$ in the backward Euler method. Equation (10) must then be solved by iteration. The standard Newton–Raphson method is adopted in this study. More details on solving Equation (9) are given by Sheng and Sloan [22].

2.3. Stress integration

For nonlinear materials, such as those represented by the Mohr–Columb or Cam–Clay models, the stress increment is usually found by integration over a given strain increment. For small deformation, the stress integration is performed as follows:

$$\begin{aligned}\sigma'^{t+\Delta t}_{ij}&=\sigma'^{t}_{ij}+\int_0^{\Delta\varepsilon_{kl}} C'_{ijkl}(\sigma',\kappa)\,\mathrm{d}\varepsilon_{kl}\\ \kappa_i^{t+\Delta t}&=\kappa_i^{t}+\int_0^{\Delta\varepsilon_{kl}} B_i(\sigma',\kappa)\,\mathrm{d}\lambda=\kappa_i^{t}+\int_0^{\Delta\varepsilon_{kl}} B_i(\sigma',\kappa)\cdot D_{kl}(\sigma',\kappa)\,\mathrm{d}\varepsilon_{kl}\end{aligned} \tag{11}$$

where κ_i is a set of hardening parameters, C' is the constitutive matrix depending on the current stresses and hardening parameters, B is a set of variables derived from the hardening law and is typically a function of the current stresses and hardening parameters, $\mathrm{d}\lambda$ is the plastic multiplier that depends on the strain rate, and D is a vector derived from the consistency condition and the flow rule and is again a function of the current stresses and hardening parameters.

For a large deformation analysis, the stress integration is no longer governed by Equation (11), due to possible rigid body rotation. In the UL formulation based on the Jaumann stress rate, the effective stress increment is found by integrating $\mathrm{d}\sigma'$ in Equation (3) for a given strain increment, i.e.

$$\sigma'^{t+\Delta t}_{ij}=\sigma'^{t}_{ij}+\int_0^{\Delta\varepsilon_{ij}}\mathrm{d}\sigma'_{ij}=\sigma'^{t}_{ij}+\int_0^{\Delta\varepsilon_{kl}} C'_{ijkl}(\sigma')\,\mathrm{d}\varepsilon_{kl}+\int_0^{\Delta\Omega_{kl}}(\sigma'_{ik}\,\mathrm{d}\Omega_{jk}+\sigma'_{jl}\,\mathrm{d}\Omega_{il}) \tag{12}$$

where $C'(\sigma')$ refers to the constitutive matrix with respect to the configuration at time t and is a function of the current Cauchy stresses. Equation (12) shows that the stress-integration schemes used for small deformation have to be modified to include the additional terms due to rigid body rotation. Considering the skew-symmetry of $\Delta\Omega_{ij}$, it is possible to show that the second integration

DOI: 10.1002/nag

in (12) is equivalent to a stress transformation:

$$\sigma'^{t}_{ij} + \int_0^{\Delta\Omega_{kl}} (\sigma'_{ik}\,\mathrm{d}\Omega_{kj} + \sigma'_{jl}\,\mathrm{d}\Omega_{li}) = Q_{ik}\sigma'^{t}_{kl}Q_{jl} \tag{13}$$

with

$$Q_{ij} = (\delta_{ik} - \alpha\Delta\Omega_{ik})^{-1}(\delta_{kj} + (1-\alpha)\Delta\Omega_{kj})$$

where α is an integration parameter varying between 0 and 1. One key requirement for a stress-integration scheme for large deformation is that it should be objective, meaning that the stress transformation (13) should not cause any straining. Hughes and Winget [23] showed that the stress transformation (13) is objective if Q is orthogonal, and that the orthogonality of Q exists provided the strain increment and the spin tensor increment are evaluated with respect to the configuration at the midpoint $t + \Delta t/2$ and $\alpha = 0.5$. Under these conditions, the stress integration can be carried out as

$$\begin{aligned} \sigma'^{t+\Delta t}_{ij} &= Q_{ik}\sigma'^{t}_{kl}Q_{jl} + \int_0^{\Delta\varepsilon_{kl}} C_{ijkl}(\sigma')\,\mathrm{d}\varepsilon_{kl} \\ \kappa_i^{t+\Delta t} &= \kappa_i^t + \int_0^{\Delta\varepsilon_{kl}} B_i(\sigma', \kappa)\cdot D_{kl}(\sigma', \kappa)\,\mathrm{d}\varepsilon_{kl} \end{aligned} \tag{14}$$

The integration in (14) is almost identical to the integration in (11) for small deformation. The only modification is that the stresses at the start of the increment should be transformed according to (13). Therefore, standard integration schemes used for small deformation can also be used to update the stresses and hardening parameters in (14). In this study, an explicit scheme based on the work by Sloan *et al.* [24] is used. This stress-integration scheme controls the error in the computed stresses by using a local error measure to automatically subincrement the applied strain increment. The error measure is computed at each integration point by taking the difference between a first-order accurate Euler solution and a second-order accurate modified Euler solution. The method has been used to solve problems involving a wide range of constitutive models for soils and has been generalized by Nazem *et al.* [14] for large deformations.

2.4. Porosity and permeability updates

The permeability of a soil depends on its porosity and the latter changes as deformation occurs. To study the variation of porosity, let n^t and V^t represent, respectively, the porosity and volume of a material point at time t. The volumes of the voids and the solids at time t are, respectively,

$$\begin{aligned} V_{\mathrm{v}}^t &= n^t \cdot V^t \\ V_{\mathrm{s}}^t &= (1 - n^t) \cdot V^t \end{aligned} \tag{15}$$

As the soil skeleton deforms, its volume at time $t + dt$ will be

$$V^{t+\Delta t} = J \cdot V^t \tag{16}$$

Since a soil particle is assumed to be incompressible, i.e.

$$V_{\mathrm{s}}^{t+\Delta t} = V_{\mathrm{s}}^t \tag{17}$$

DOI: 10.1002/nag

the new volume of the voids will be

$$V_{\mathrm{v}}^{t+\Delta t} = V^{t+\Delta t} - V_{\mathrm{s}}^{t+\Delta t} = V^{t+\Delta t} - V_{\mathrm{s}}^{t} = J \cdot V^{t} - (1 - n^{t}) \cdot V^{t} \tag{18}$$

The porosity at time $t + \Delta t$ can then be obtained using

$$n^{t+\Delta t} = \frac{V_{\mathrm{v}}^{t+\Delta t}}{V^{t+\Delta t}} = \frac{J \cdot V^{t} - (1 - n^{t}) \cdot V^{t}}{J \cdot V^{t}} = 1 - \frac{1 - n^{t}}{J} \tag{19}$$

Note that if deformation is small so that $J \approx 1$ in Equation (19), the porosity will then be constant during the analysis, i.e. $n^{t+\Delta t} = n^{t}$. Equation (19) shows that in large deformation analysis the porosity should be updated as the body deforms and its volume changes. Usually it is more convenient to deal with the voids ratio instead of the porosity in geomechanics. On the basis of Equation (19), a relationship can be found for the void ratio update according to

$$e^{t+\Delta t} = \frac{n^{t+\Delta t}}{1-n^{t+\Delta t}} = \frac{1-\dfrac{1-n^{t}}{J}}{1-\left(1-\dfrac{1-n^{t}}{J}\right)} = \frac{J-1+n^{t}}{1-n^{t}} = \frac{J-1+\dfrac{e^{t}}{1+e^{t}}}{1-\dfrac{e^{t}}{1+e^{t}}} = J(1+e^{t})-1 \tag{20}$$

where e is the voids ratio. Alternatively, we can derive Equation (20) by using the definition of the voids ratio

$$e^{t+\Delta t} = \frac{V_{\mathrm{v}}^{t+\Delta t}}{V_{\mathrm{s}}^{t+\Delta t}} = \frac{V^{t+\Delta t} - V_{\mathrm{s}}^{t+\Delta t}}{V_{\mathrm{s}}^{t+\Delta t}} = \frac{V^{t+\Delta t}}{V_{\mathrm{s}}^{t+\Delta t}} - 1 = \frac{V^{t+\Delta t}}{V^{t}} \cdot \frac{V^{t}}{V_{\mathrm{s}}^{t}} \cdot \frac{V_{\mathrm{s}}^{t}}{V_{\mathrm{s}}^{t+\Delta t}} - 1 = J(1+e^{t})J_{\mathrm{s}}^{-1} - 1 \tag{21}$$

The voids ratio is usually updated and stored at integration points and is therefore a state parameter like the stresses and strains.

The permeability is usually a function of the voids ratio or porosity. Such a function is typically obtained by curve-fitting experimental data and depends on the type of the soil. One such function is the Kozeny–Carman equation [25]

$$k = C_1 \frac{e^{\alpha}}{1 + e} \tag{22}$$

in which C_1 is a parameter that depends on the viscosity of the permeant, the specific surface area and the pore shape of the soil, and is usually determined experimentally. The parameter α depends on the soil type and is typically set to 3 for granular soils. For clays, a logarithmic equation is used [26]

$$\log k = \log k_0 - \frac{e_0 - e}{C_k} \tag{23}$$

where C_k is a soil parameter that is approximately equal to $0.5e_0$ and k_0 is the *in situ* coefficient of permeability at the voids ratio e_0.

Another important factor that changes the permeability in large deformation analysis is rigid body rotation of an element of soil. If the soil is anisotropic, the permeability tensor changes due to rigid body rotation and must be considered in the analysis. Figure 1(a) shows the configuration of a material point at time t in the x–y system of coordinates. The point is then rotated by θ degrees and is shown again in Figure 1(b) and (c) at time $t + \Delta t$ in the $\overline{x} - \overline{y}$ system of coordinates.

DOI: 10.1002/nag

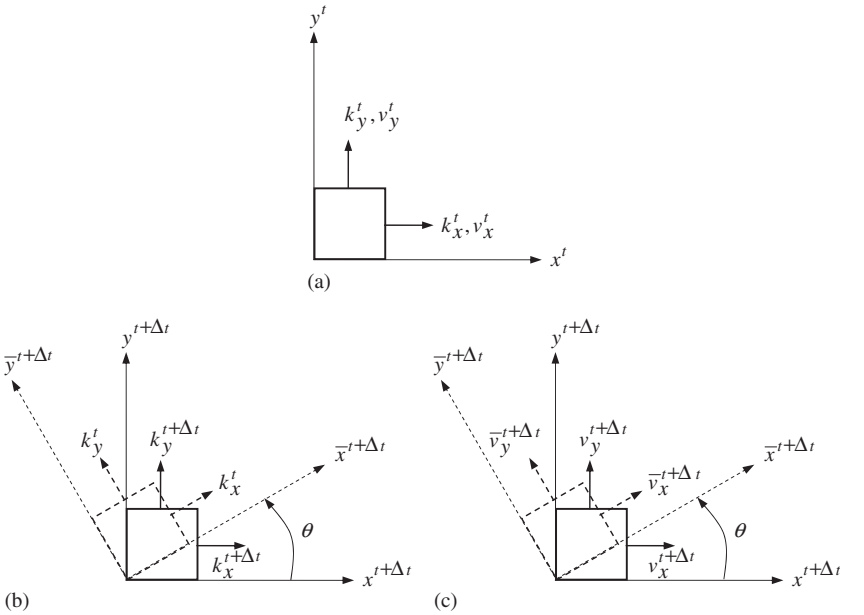

Figure 1. Configuration at time t and $t+\Delta t$: (a) permeabilities and velocities at time t; (b) permeabilities at time $t+\Delta t$; and (c) velocities at time $t+\Delta t$.

We first assume that rigid body rotation is the only deformation mechanism during this time interval. Darcy's law at time t and $t+dt$ can then be written, respectively, as follows:

$$n^t(v_{\mathrm{w}i}^t - v_{\mathrm{s}i}^t) = -k_{ij}^t \frac{\partial h^t}{\partial x_j} \tag{24}$$

$$n^{t+\Delta t}(\overline{v}_{\mathrm{w}i}^{t+\Delta t} - \overline{v}_{\mathrm{s}i}^{t+\Delta t}) = -k_{ij}^t \frac{\partial h^{t+\Delta t}}{\partial \overline{x}_j^{t+\Delta t}} \tag{25}$$

where h is the hydraulic head. The rigid body rotation does not change the porosity, i.e. $n^{t+\Delta t} = n^t$, and we can define the rotation by the rotation tensor, R, i.e.

$$\overline{x}_i^{t+\Delta t} = R_{ij} x_i^{t+\Delta t} \tag{26}$$

It is easy to show that in the case of pure rigid body rotation (i.e. without straining),

$$F_{ij} = R_{ij} = \begin{bmatrix} \cos\theta & -\sin\theta \\ \sin\theta & \cos\theta \end{bmatrix} \tag{27}$$

We also notice that

$$\frac{\partial h^{t+\Delta t}}{\partial \overline{x}_i^{t+\Delta t}} = R_{ij} \frac{\partial h^{t+\Delta t}}{\partial x_j^{t+\Delta t}} \tag{28}$$

DOI: 10.1002/nag

and

$$\overline{v}_i^{t+\Delta t} = R_{ij} \cdot v_j^{t+\Delta t} \tag{29}$$

Substituting Equations (28) and (29) into Equation (25) gives

$$n^{t+\Delta t} \cdot R_{ij} \cdot (v_{\mathrm{w}j}^{t+\Delta t} - v_{\mathrm{s}j}^{t+\Delta t}) = -k_{ij}^{t} \cdot R_{jk} \cdot \frac{\partial h^{t+\Delta t}}{\partial x_k^{t+\Delta t}} \tag{30}$$

Multiplying both sides of Equation (30) by R^{-1} and noting $R^{-1} = R^{\mathrm{T}}$ leads to

$$n^{t+\Delta t} \cdot (v_{\mathrm{w}i}^{t+\Delta t} - v_{\mathrm{s}i}^{t+\Delta t}) = -k_{ij}^{t+\Delta t} \cdot \frac{\partial h^{t+\Delta t}}{\partial x_j^{t+\Delta t}} \tag{31}$$

where

$$k_{ij}^{t+\Delta t} = R_{ik}^{\mathrm{T}} \cdot k_{kl}^{t} \cdot R_{lj} \tag{32}$$

Equation (32) gives the change in permeability due to rigid body rotation.

3. ARBITRARY LAGRANGIAN–EULERIAN FORMULATION

3.1. ALE preliminaries

Mesh distortion is the main drawback of the UL method and it can cause divergence and inaccuracy in the analysis. The ALE method has been developed to overcome this drawback by separating the mesh from the material points.

A study of the ALE method and its performance in geotechnical problems has recently been presented by Nazem *et al*. [14] and Nazem and Sheng [27], where the ALE method based on the operator-split technique is shown to be effective in handling the mesh distortion of Lagrangian methods. The same technique is used here to solve coupled finite element problems. To solve the coupled governing equations by the operator-split technique, two steps are considered in the analysis: a UL step followed by a Eulerian step. In the UL step, we solve the coupled equilibrium and mass conservation equations to obtain the material displacements. At the end of the UL step, the mesh may be distorted. In the Euler step, a new and better mesh is generated for the deformed domain to obtain the mesh displacements. All kinematic and static variables are then transferred from the distorted mesh to the new mesh. The key issues in the operator-split ALE method thus include the mesh generation in the Euler step and the remapping of variables between the two meshes. The remapping of the variables is usually done using the convection equation [28]

$$\dot{f}^r = \dot{f} + (v_i - v_i^r)\frac{\partial f}{\partial x_i} \tag{33}$$

where $\dot{f}^r$ and $\dot{f}$ denote the time derivatives of an arbitrary function f with respect to the mesh and material coordinates, respectively, v_i is the material velocity and v_i^r represents the mesh velocity.

DOI: 10.1002/nag

3.2. Mesh movement and mesh optimization

The transformation of state variables by the convection equation (Equation (33)) requires the determination of mesh movement. To compute the convective velocity, $v - v^r$, knowledge of the material displacements and mesh displacements is necessary. The material displacements are obtained at the end of the UL step. A new and undistorted mesh is then generated for the deformed domain from which the mesh displacements can be found. This procedure basically requires various mesh-generation algorithms that must consider several factors such as the dimension of the problem, the type of elements to be generated and the regularity of the domain. Developing such algorithms to cover arbitrary conditions is cumbersome and costly. A simple and effective method for determining the mesh displacements based on the elastic analysis is explained in detail here. This method was originally developed by Nazem and Sheng [27] for two-dimensional plane strain problems and axi-symmetric problems. The method is based on the observation that mesh distortions do not usually occur in the analysis of problems with isotropic elastic materials. This assumption motivates the development of a mesh optimization technique based on elastic analysis. It must be noted that the boundaries of the problem must not be changed during the procedure of mesh optimization. However, the nodes can be relocated along the boundaries to decrease the mesh distortion. The procedure of mesh optimization includes two steps: relocation of nodes along the boundaries and an elastic analysis that will be explained in the following. The main advantage of this technique is that it can be easily implemented in existing finite element codes since the necessary information for an elastic analysis is already available. Moreover, the method does not take advantage of any complicated mathematical algorithms (such as Laplacian smoothing) for mesh optimization.

3.2.1. Relocation of nodes along boundaries. As mentioned earlier, mesh displacements and material displacements are uncoupled in the operator-split ALE method. The material displacements are obtained from the UL step. To obtain the mesh displacements, all boundaries are first re-discretized, which include the boundaries of the domain, the material interfaces and the loading boundaries. This procedure is depicted in Figure 2. Supposing the nodes on the undeformed boundaries (Figure 2(a)) are distorted after the UL step as shown in Figure 2(b), these nodes are then relocated on the deformed boundaries as shown in Figure 2(c). It should be noted that the normal component

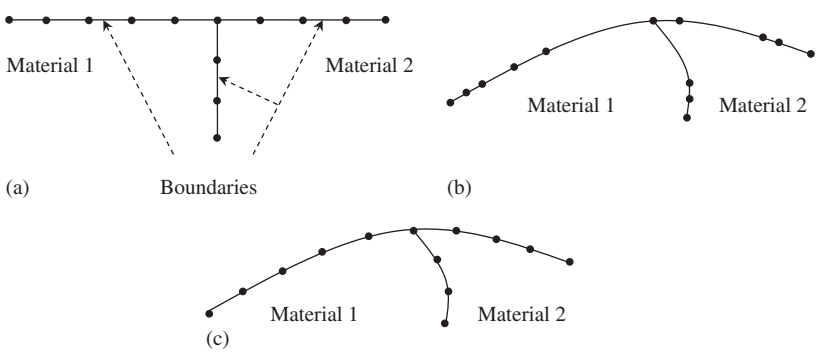

Figure 2. Relocation of nodes on the boundaries in two-dimensional cases: (a) boundaries before deformation; (b) boundaries after deformation; and (c) boundaries after relocation of nodes.

DOI: 10.1002/nag

of the convective velocity on a boundary is zero, but not necessarily the tangential component. Therefore, the tangential component of the convective velocity must be considered when redefining the positions of these nodes.

The relocation of the nodes requires a mathematical representation of the boundaries. A naive approach is to use Lagrange polynomials, which will introduce large computational errors if the number of nodes on a boundary is large (normally greater than 10). A more convenient and accurate method is the quadratic spline technique [29] which divides the boundary into a number of quadratic functions. Supposing there are n nodes on an arbitrary boundary with global coordinates x_i and y_i, the polynomial defining this boundary can then be written by k quadratic functions as

$$y = \begin{cases} \displaystyle\sum_{i=1}^{3} \left(y_i \cdot \prod_{\substack{j=1 \\ j\neq i}}^{3} \frac{(x - x_j)}{(x_i - x_j)} \right) = A_1 \cdot x^2 + B_1 \cdot x + C_1, & x_1 \leqslant x \leqslant x_3 \\ \displaystyle\sum_{i=3}^{5} \left(y_i \cdot \prod_{\substack{j=3 \\ j\neq i}}^{5} \frac{(x - x_j)}{(x_i - x_j)} \right) = A_2 \cdot x^2 + B_2 \cdot x + C_2, & x_3 \leqslant x \leqslant x_5 \\ \vdots & \\ \displaystyle\sum_{i=n-2}^{n} \left(y_i \cdot \prod_{\substack{j=n-2 \\ j\neq i}}^{n} \frac{(x - x_j)}{(x_i - x_j)} \right) = A_k \cdot x^2 + B_k \cdot x + C_k, & x_{n-2} \leqslant x \leqslant x_n \end{cases} \tag{34}$$

where

$$k = \frac{n-1}{2} \tag{35}$$

For boundaries including quadratic elements, n is an odd number and subsequently k will be an integer number. The length of an arbitrary segment defined by $y = A_i \cdot x^2 + B_i \cdot x + C_i$, where $x_{2i-1} \leqslant x \leqslant x_{2i+1}$, is denoted by L_i and may be obtained as follows:

$$L_i = \int_{x_{2i-1}}^{x_{2i+1}} \sqrt{1 + \left(\frac{\mathrm{d}y}{\mathrm{d}x} \right)^2} \, \mathrm{d}x \tag{36}$$

Performing the integration in (36) explicitly, L_i is given by

$$L_i = f_1(x_{2i+1}) - f_1(x_{2i-1}) \tag{37}$$

where

$$f_1(x) = \frac{1}{4A_i} ((2A_i \cdot x + B_i) \cdot f_2(x) + \ln |2A_i \cdot x + B_i + f_2(x)|) \tag{38}$$

and

$$f_2(x) = \sqrt{4A_i^2 \cdot x^2 + 4A_i \cdot B_i \cdot x + B_i^2 + 1} \tag{39}$$

DOI: 10.1002/nag

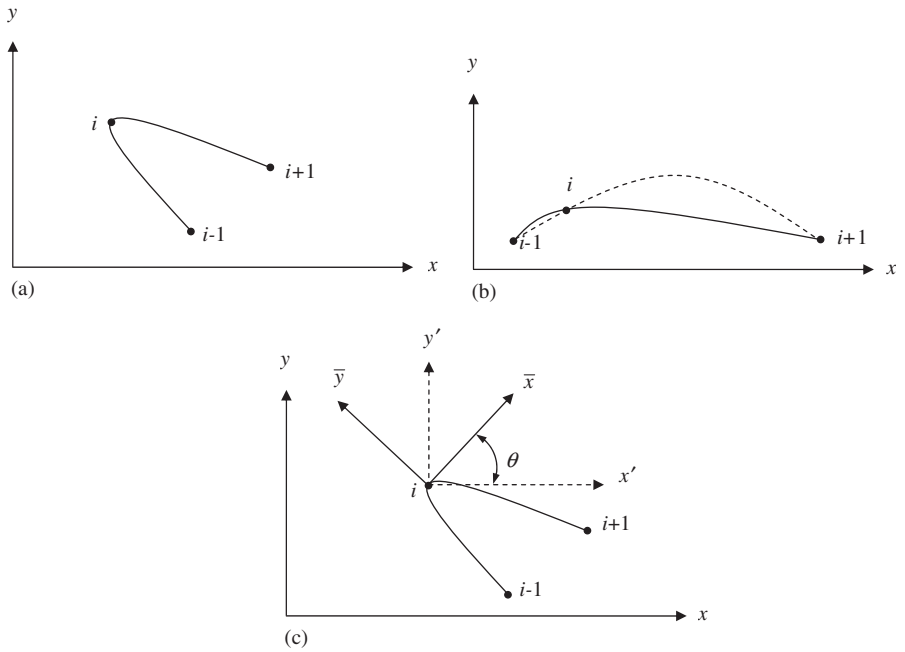

Figure 3. Spline interpolation technique and its refinement: (a) special case 1; (b) special case 2; and (c) translation and rotation of the axes.

The total length of the boundary, L, is simply the summation of the lengths of each segment, hence

$$L = \sum_{i=1}^{k} L_i \tag{40}$$

Knowing the length of the boundary, it is easy to redivide it to obtain a set of new nodes, redistributed spatially in some desired fashion. For simplicity, a vector of normalized lengths l_i may be defined where the length between two successive nodes i and $i+1$ is given by $L \cdot l_i$.

The quadratic interpolation (34) provides no solution for the special case where a segment of the boundary with three respective nodes $i-1$, i and $i+1$ satisfies the conditions $x_i < x_{i-1} < x_{i+1}$ and $y_{i-1} < y_{i+1} < y_i$, as depicted in Figure 3(a). In this case no explicit expression in one of the standard forms $y = f(x)$ or $x = f(y)$ can be obtained by Equation (34). Moreover, if the middle point of a segment is too close to one of the corner nodes, the curve approximated by Equation (34) does not represent an accurate estimation of the real boundary. This drawback is shown in Figure 3(b) where the real segment is plotted as a solid line and the dashed line represents the quadratic estimation. In this case, the length of the segment and consequently the total length of the boundary includes a significant error that results in a poor relocation of the nodes. More importantly, the nodes may leave the original boundary producing a non-zero normal component of the convective velocity across the boundary.

To overcome these two drawbacks, the origin of the Cartesian system is moved to node i and the axes are then rotated by θ degrees about the new origin, as depicted in Figure 3(c). This translation and rotation introduces two new systems of coordinates denoted by $(x' - y')$ and $(\overline{x} - \overline{y})$, respectively. The angle θ may be determined by assuming $\overline{x}$ is tangent to the segment at node i.

DOI: 10.1002/nag

In other words, node i will be chosen as a minimum (or maximum) point of the segment in $(\overline{x}-\overline{y})$ coordinates. The quadratic function describing the segment in $(\overline{x}-\overline{y})$ coordinates can then be expressed as

$$\overline{y}=\overline{A}\cdot\overline{x}^2 \tag{41}$$

where $\overline{A}$ is a constant to be determined and

$$\begin{Bmatrix}\overline{x}\\ \overline{y}\end{Bmatrix}=\begin{bmatrix}\cos\theta & \sin\theta\\ -\sin\theta & \cos\theta\end{bmatrix}\begin{Bmatrix}x'\\ y'\end{Bmatrix} \tag{42}$$

in which

$$\begin{aligned}x'&=x-x_i\\ y'&=y-y_i\end{aligned} \tag{43}$$

By substituting the coordinates of nodes $i-1$ and $i+1$ into Equation (41) and using these two equations to eliminate $\overline{A}$, one obtains

$$\overline{y}_{i-1}\cdot\overline{x}_{i+1}^2-\overline{y}_{i+1}\cdot\overline{x}_{i-1}^2=0 \tag{44}$$

Transforming this equation to the $(x'-y')$ system of coordinates yields the expression

$$\begin{aligned}&(-\sin\theta\cdot x'_{i-1}+\cos\theta\cdot y'_{i-1})(\cos\theta\cdot x'_{i+1}+\sin\theta\cdot y'_{i+1})^2\\ &\quad-(-\sin\theta\cdot x'_{i+1}+\cos\theta\cdot y'_{i+1})(\cos\theta\cdot x'_{i-1}+\sin\theta\cdot y'_{i-1})^2=0\end{aligned} \tag{45}$$

Expanding Equation (42) and summarizing the resulting expression lead to the following trigonometric equation:

$$M\cdot\tan\theta^3+N\cdot\tan\theta^2+P\cdot\tan\theta+Q=0 \tag{46}$$

where

$$\begin{aligned}M&=-x'_{i-1}\cdot y'^2_{i+1}+x'_{i+1}\cdot y'^2_{i-1}\\ N&=y'_{i-1}\cdot x'^2_{i+1}-y'_{i+1}\cdot x'^2_{i-1}\\ P&=(y'_{i-1}-y'_{i+1})(2x'_{i-1}\cdot x'_{i+1}-y'_{i-1}\cdot y'_{i+1})\\ Q&=(x'_{i-1}-x'_{i+1})(x'_{i-1}\cdot x'_{i+1}-2y'_{i-1}\cdot y'_{i+1})\end{aligned} \tag{47}$$

Equation (46) has at least one real root that can be explicitly computed without performing a numerical solution. Therefore, θ is given

$$\theta=-\arctan\left[\frac{1}{3M}\left(N-\frac{\sqrt[3]{R^2}+4(3P\cdot M-N^2)}{2\sqrt[3]{R}}\right)\right] \tag{48}$$

where

$$\begin{aligned}R&=36M\cdot N\cdot P-108Q\cdot M^2-8N^3\\ &\quad+12\sqrt{3(4M\cdot P^3-N^2\cdot P^2-18M\cdot N\cdot P\cdot Q+27M^2\cdot Q^2+4M\cdot Q\cdot N^3)}\end{aligned} \tag{49}$$

DOI: 10.1002/nag

Once θ is found, substituting the $(\overline{x}-\overline{y})$ coordinates of node $i-1$ (or node $i+1$) into Equation (41) and solving for $\overline{A}$ gives

$$\overline{A}=\frac{-\sin\theta\cdot x'_{i-1}+\cos\theta\cdot y'_{i-1}}{(\cos\theta\cdot x'_{i-1}+\sin\theta\cdot y'_{i-1})^2}=\frac{-\sin\theta\cdot x'_{i+1}+\cos\theta\cdot y'_{i+1}}{(\cos\theta\cdot x'_{i+1}+\sin\theta\cdot y'_{i+1})^2} \tag{50}$$

The functions defining the boundary can now be written in the following form:

$$\overline{y}=\begin{cases}\overline{A}_1\cdot\overline{x}^2, & \overline{x}_1\leqslant\overline{x}\leqslant\overline{x}_3\\ \overline{A}_2\cdot\overline{x}^2, & \overline{x}_3\leqslant\overline{x}\leqslant\overline{x}_5\\ \vdots & \\ \overline{A}_k\cdot\overline{x}_k^2, & \overline{x}_{n-2}\leqslant\overline{x}\leqslant\overline{x}_n\end{cases} \tag{51}$$

An algorithm that relocates the nodes on a boundary by the method explained above is summarized below. This algorithm computes the length of a segment and the total length of a boundary and then uses the bisection method to find the new position of nodes.

Algorithm 1 (*Nodal relocation across a boundary*)

(1) Enter with number of nodes on the boundary n, global coordinates of each nodes (x_i and y_i), and the normalized lengths l_i $(1\leqslant i\leqslant n-1)$.
(2) Allocate memory for temporary coordinates x_i^* and y_i^* $(1\leqslant i\leqslant n-2)$.
(3) Set $k=(n-1)/2$ and perform steps 4–7 for $i=1$ to k.
(4) Compute x'_{2i+j} and y'_{2i+j} for $j=-1, 0, 1$ using

$$x'_{2i+j}=x_{2i+j}-x_{2i}$$

$$y'_{2i+j}=y_{2i+j}-y_{2i}$$

(5) Find θ_i by Equation (48) and the parameters defined in (47), then calculate $\overline{A}_i$ using Equation (50).
(6) Compute $\overline{x}_{2i+j}$ and $\overline{y}_{2i+j}$ for $j=-1$ and 1 using

$$\begin{Bmatrix}\overline{x}_{2i+j}\\ \overline{y}_{2i+j}\end{Bmatrix}=\begin{bmatrix}\cos\theta_i & \sin\theta_i\\ -\sin\theta_i & \cos\theta_i\end{bmatrix}\begin{Bmatrix}x'_{2i+j}\\ y'_{2i+j}\end{Bmatrix}$$

(7) Calculate the length of quadratic spline:

$$L_i=\overline{f}_1(\overline{x}_{2i+1})-\overline{f}_1(\overline{x}_{2i-1})$$

$$\overline{f}_1(x)=\frac{1}{4\overline{A}_i}(2\overline{A}_i\cdot x\cdot\overline{f}_2(x)+\ln|2\overline{A}_i\cdot x+\overline{f}_2(x)|)$$

$$\overline{f}_2(x)=\sqrt{4\overline{A}_i^2\cdot x^2+1}$$

DOI: 10.1002/nag

(8) Find the total length of the boundary L by $L = \sum_{i=1}^{k} L_i$.
(9) Perform steps 10–15 for $i = 1$ to $n - 2$.
(10) Set $X_1 = x_1$ and $X_2 = x_n$.
(11) If $i > 1$, then set $X_1 = x^*_{i-1}$.
(12) Set $x_s = X_1$.
(13) Calculate $x_t = (X_1 + X_2)/2$ and find the length of the boundary between x_s and x_t and store it in L_s.
(14) If $|L_s - L \cdot l_i| \leqslant$PREC, first set $x^*_i = x_t$, compute the correspondent y^*_i and then set $i \leftarrow i+1$ before returning to step 10.
(15) If $L_s < L \cdot l_i$, then

$$X_1 = x_t$$

else

$$X_2 = x_t$$

Endif.
Go to step 13.
(16) Set $x_{i+1} = x^*_i$ and $y_{i+1} = y^*_i$ for $i = 1$ to $n - 2$.
(17) Exit with the new global coordinates x_i and y_i.

Note that equations given in step 7 are the special cases of Equations (37)–(39) when $B_i = 0$. In addition, the variable PREC in step 14 is a parameter representing the precision of the nodal relocation and is typical in the range of 10^{-3}–10^{-6}.

3.2.2. Mesh refinement by elastic analysis. The UL step in the operator-split technique is performed to obtain the material displacements. The incremental material displacements Δu_i and subsequently the locations of material points $x_i^{t+\Delta t}$ are known at the end of this step. However, the resulting mesh can often be distorted. Relocation of nodes, as explained in the previous section, provides the locations of mesh points $(x_i^r)^{t+\Delta t}$ only for those on the boundaries. Therefore, the incremental mesh displacements Δu_i^r for all nodes on the boundaries may be obtained by

$$\Delta u_i^r = (x_i^r)^{t+\Delta t} - x_i^{t+\Delta t} + \Delta u_i \tag{52}$$

Mesh distortions can be removed by refining the mesh by simply relocating the interior nodes. With known displacements Δu_i^r of the nodes on the boundaries, an elastic analysis is performed using the mesh at time t and Δu_i^r as the prescribed displacements along the boundaries. This analysis assumes isotropic linear elasticity of a homogeneous medium and small deformation theory and aims to find Δu_i^r for internal nodes. Because the displacements are prescribed along all boundaries and material interfaces, the actual values of the elastic parameters used in this analysis are not important and one set of elastic parameters can be used for the entire domain, regardless of the presence of real material interfaces. The incremental displacement components computed for each node from this elastic analysis are then added to the nodal coordinates of the mesh at time t to define the locations of the nodes in the new mesh at time $t + \Delta t$ by

$$(x_i^r)^{t+\Delta t} = x_i^t + \Delta u_i^r \tag{53}$$

The new mesh and the mesh at time t share the same connectivity. Such an elastic analysis should result in an optimal mesh if the nodes on the boundaries are optimally located. More importantly,

DOI: 10.1002/nag

such an analysis is very fast to complete, compared with the use of mesh generation processes, e.g. by triangulation.

3.3. Remapping state variables

In general, two sets of variables must be transformed by the convection equation (33) once the mesh displacements are known: variables at integration points (such as stresses, hardening parameters and permeabilities) and variables at nodal points (such as pore-water pressures). Although the same equation is used for remapping both sets of variables, the procedures are, however, different. Remapping the variables at integration points is explained here, with the stresses used as an example. Multiplying Equation (33) by the time increment and substituting the effective stresses for function f leads to

$$\sigma'^{r}_{ij} = \sigma'_{ij} + (u^r_k - u_k) \cdot \frac{\partial \sigma'_{ij}}{\partial x_k} \tag{54}$$

where σ'^{r}'s are the effective stresses at the Gauss points of the new mesh and σ''s are the corresponding values for the old mesh. To find the gradient of an arbitrary component of the effective stresses in Equation (54), we may write

$$\frac{\partial \sigma'}{\partial x_i} = \frac{\partial \sigma'}{\partial \xi} \cdot \frac{\partial \xi}{\partial x_i} + \frac{\partial \sigma'}{\partial \eta} \cdot \frac{\partial \eta}{\partial x_i} \tag{55}$$

The above equation is valid for two-dimensional isoparametric elements. The derivatives of the effective stresses with respect to the normal coordinates, ξ and η, can be computed using the displacement shape functions N_i

$$\begin{aligned} \frac{\partial \sigma'_{ij}}{\partial \xi} &= \sum_{k=1}^{n} \frac{\partial N_k}{\partial \xi} \cdot \sigma'^{k}_{ij} \\ \frac{\partial \sigma'_{ij}}{\partial \eta} &= \sum_{k=1}^{n} \frac{\partial N_k}{\partial \eta} \cdot \sigma'^{k}_{ij} \end{aligned} \tag{56}$$

where n is the number of nodes per element and the σ'^{k} are the nodal effective stresses. To compute the nodal effective stresses, a nodal stress recovery technique can be used. In this study, the super-convergent patch recovery technique developed by Zienkiewicz and Zhu [30] is used. This method assumes that the stress values in a patch are computed using a polynomial of the same order as the displacement shape functions. For more details, see Zienkiewicz and Zhu [30].

To remap the state variables at nodal points, such as the pore-water pressures, we again use Equations (54) and (55) with the effective stresses σ' and σ'^{r} replaced by the corresponding pore-water pressures p and p^r, respectively. Equation (56) is then rewritten in terms of the pore pressure shape functions N_{pi},

$$\begin{aligned} \frac{\partial p_{ij}}{\partial \xi} &= \sum_{k=1}^{m} \frac{\partial N_{pk}}{\partial \xi} \cdot p^k_{ij} \\ \frac{\partial p_{ij}}{\partial \eta} &= \sum_{k=1}^{m} \frac{\partial N_{pk}}{\partial \eta} \cdot p^k_{ij} \end{aligned} \tag{57}$$

DOI: 10.1002/nag

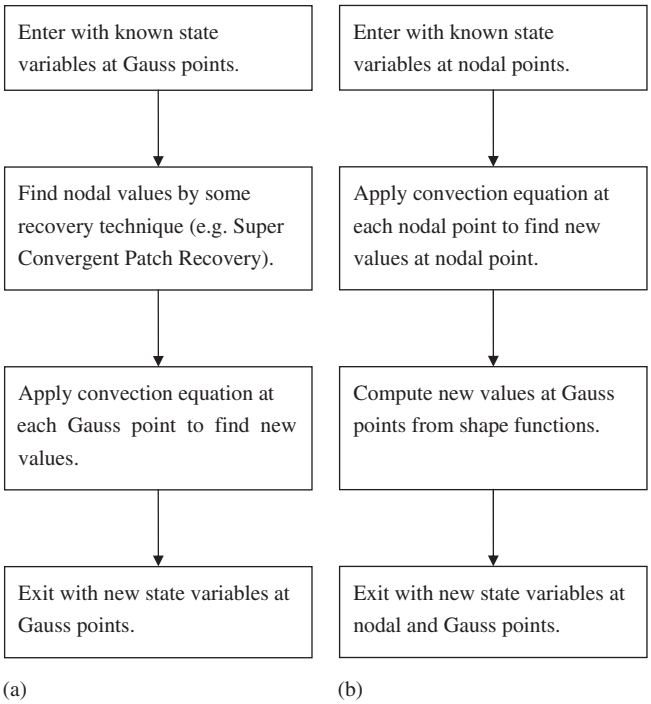

Figure 4. Remapping state variables: (a) at Gauss points and (b) at nodal points.

where m represents the number of pore pressure nodes per element and p^k are the nodal pore pressures that are known from the UL step. Here no nodal recovery procedure is required. The convection equation is applied at the pore pressure nodes of each element. Finally, the new values of pore-water pressures at integration points are computed by the interpolation functions.

The above two procedures for remapping state variables at integration points and nodes are shown schematically in Figure 4.

3.4. Equilibrium check

The transformation of state parameters between the old mesh and the new mesh is not guaranteed to be objective. As such, the global equilibrium and the local consistency conditions may be violated after the transformation. To the authors' knowledge, there is no simple solution to this problem available in the literature. Therefore, the global equilibrium and the local consistency must be checked again. To bring the system to equilibrium, additional Newton–Raphson iterations may be needed, and test runs indicate that typically 2–5 iterations are required to reduce the unbalanced forces to tolerably small values. If the remapping of the stresses and hardening parameters causes the consistency condition to be violated at the integration points, the drift correction scheme described in Sloan *et al*. [24] is used to bring the stresses back to the yield surface.

DOI: 10.1002/nag

4. NUMERICAL EXAMPLES

The UL and the ALE methods explained in the previous sections have been implemented into the finite element code, SNAC, developed at the University of Newcastle, Australia. This code is used for all the numerical examples presented in this section. Six-noded triangular isoparametric elements, with two displacement degrees of freedom at each node and one pore-water pressure degree of freedom at each corner node, are used in all problems.

Although the methods described in this paper can be used to analyze general types of large deformation problems in geomechanics, we limit our applications here to cavity expansion and elastoplastic consolidation of a footing with hardening and non-hardening materials. Consolidation problems involving large deformations have also been addressed by others, e.g. Carter *et al.* [2, 3], Zienkiewicz and Shiomi [6], Borja and Alarcon [11], Meroi *et al.* [7], Borja *et al.* [12] and Zienkiewicz *et al.* [31]. In all these studies, the UL method has been used to obtain a solution.

4.1. Elastoplastic cylindrical cavity expansion

Cavity expansion is one of the few problems for which an analytical finite-strain plasticity solution exists in the literature. To validate the finite element formulation, the expansion of a long cylindrical cavity in an infinite medium is studied here. The problem, boundary conditions and material properties are shown in Figure 5(a). Note that, because of the plane strain formulation used, a quarter of the circle has to be used to model the cavity expansive. The internal radius of the cavity and the thickness of the soil layer are assumed to be a_0 and $60a_0$, respectively. The theoretical solution of this problem assumes an infinite medium. To simulate this, a correcting elastic layer is added to the soil layer [32]. In Figure 5(a), c is the cohesion of soil and ϕ denotes the friction angle. Note that a prime superscript and a subscript u denote the drained and undrained conditions, respectively. For a soil skeleton obeying the Mohr–Coulomb failure criterion the drained and undrained properties of the soil must satisfy the following criteria [33]:

$$E_u = \frac{3E'}{2(1+\nu')} \tag{58}$$

$$\frac{c_u}{c'} = \frac{2\sqrt{N_\phi}}{1+N_\phi} \tag{59}$$

where N_ϕ is defined by

$$N_\phi = \frac{1+\sin\phi'}{1-\sin\phi'} \tag{60}$$

The material properties of the correcting layer are those recommended by Burd [32]. Figure 5(b) represents the finite element mesh of the cavity used in this analysis. The loading includes a prescribed radial displacement of magnitude $4a_0$.

In the first analysis, the soil is assumed to behave as a Tresca material ($\phi = 0$) under undrained conditions. Only the displacement degrees of freedom are considered in this case and the results

DOI: 10.1002/nag

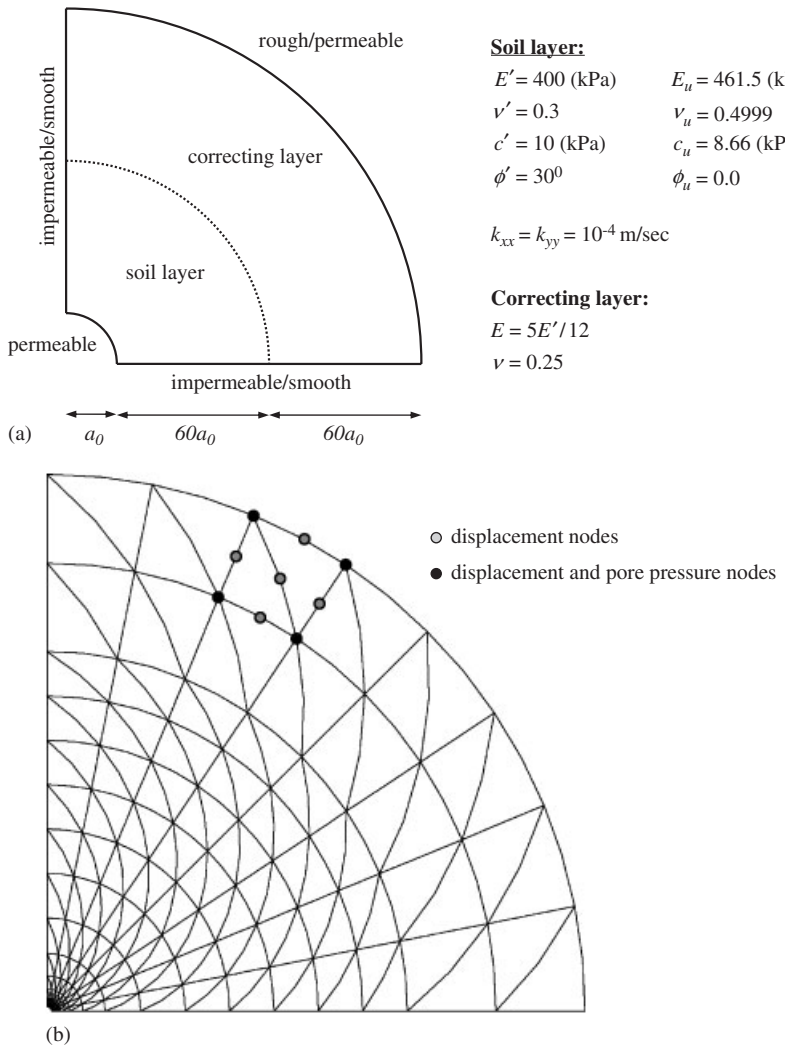

Figure 5. Cavity expansion problem: (a) geometry (not to scale), boundary conditions and material properties and (b) finite element mesh, 256 elements and 561 nodes.

are shown in Figure 6(a). The analytical solution according to Yu [34] is

$$\frac{\Psi}{c_u} = 1 + \ln\left[\frac{G}{c_u}\left(1 - \frac{a_0^2}{a^2}\right) + \frac{a_0^2}{a^2}\right] \tag{61}$$

where Ψ represents the internal pressure of the cavity, G is the shear modulus and a is the current internal radius of the cavity. Only results of the UL analysis are shown in Figure 6(a) since no serious mesh distortion is observed in this problem. Equation (61) predicts that the limit value of the ratio Ψ/c_u will be 3.87 or 3.84 when a approaches infinity or $a = 5a_0$, respectively. The numerical

DOI: 10.1002/nag

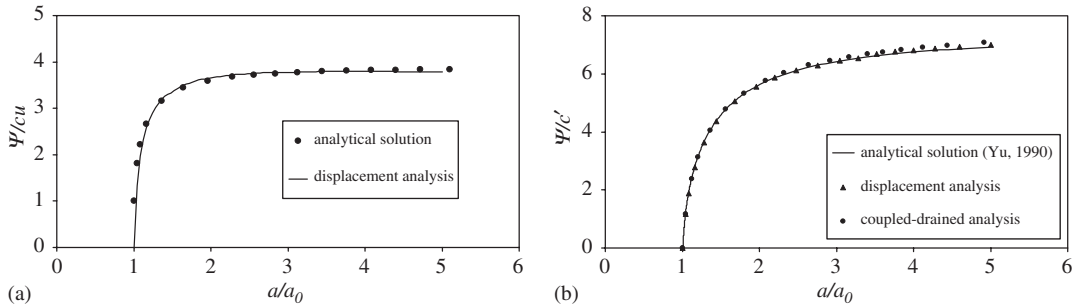

Figure 6. Normalized internal pressure of the cavity *versus* normalized radial displacement: (a) Tresca material, undrained analysis and (b) Mohr–Columb material, drained and coupled-drained analysis.

prediction of this limiting value is found to be 3.78 for a total expansion of $5a_0$. Figure 6(a) shows a good agreement between the analytical and numerical solution.

In the second type of analysis we consider the drained expansion of a cylindrical cavity in a Mohr–Columb material. The analytical solution for cavity expansion in this material is given by Yu [35] and is plotted in Figure 6(b). The results from displacement analysis and coupled analysis under drained condition are also shown in Figure 6(b). The total prescribed displacements are applied on the internal boundary over a period of 10^6 s to allow the excess pore-water pressures to dissipate fully. The limiting ratio between the cavity pressure and drained cohesion under $4a_0$ radial displacement is found to be 6.92, 7.00 and 7.09 by analytical solution, displacement analysis and coupled analysis, respectively. These values again indicate a good agreement between the analytical solution and the finite element solution.

4.2. Two-dimensional consolidation of a footing on an elastoplastic soil layer

The second example includes the analysis of a rigid strip footing resting on an elastoplatic soil layer. The problem geometry and material properties are shown in Figure 7(a), where γ represents the unit weight of the soil. Plane strain conditions are assumed and only half of the problem is considered, as depicted in Figure 7(b). The top and the bottom surfaces are assumed permeable. All the nodes under the footing are constrained in both horizontal and vertical directions to represent a rigid and rough interface.

The model is analyzed in three stages. In the first stage, body force loading due to the self-weight of the soil is applied quickly to generate a non-zero initial stress field and a hydrostatic pore pressure profile in the soil. In the second stage, a uniform pressure $q = 20$ (kPa) is applied on the footing over a period of 1 day. Finally, the load q is kept constant and the soil is allowed to consolidate over time. The analysis is continued until $t = 10^5$ (days).

Figure 8 shows the settlement *versus* time for the applied load. Both the ALE analysis and the small deformation analysis have finished with a solution, while the UL analysis terminates at time $t = 98$ days due to a negative Jacobian of some elements underneath and next to the footing edge. The ALE method predicts a final settlement of 2.35 (m), which is 5% larger than the corresponding value for the small deformation analysis (2.23 m). Note that the final settlement of the footing predicted by the ALE method is obtained after 20 000 days while the time for final settlement of the footing by small deformation analysis is 7500 days. The main reason for such a difference

DOI: 10.1002/nag

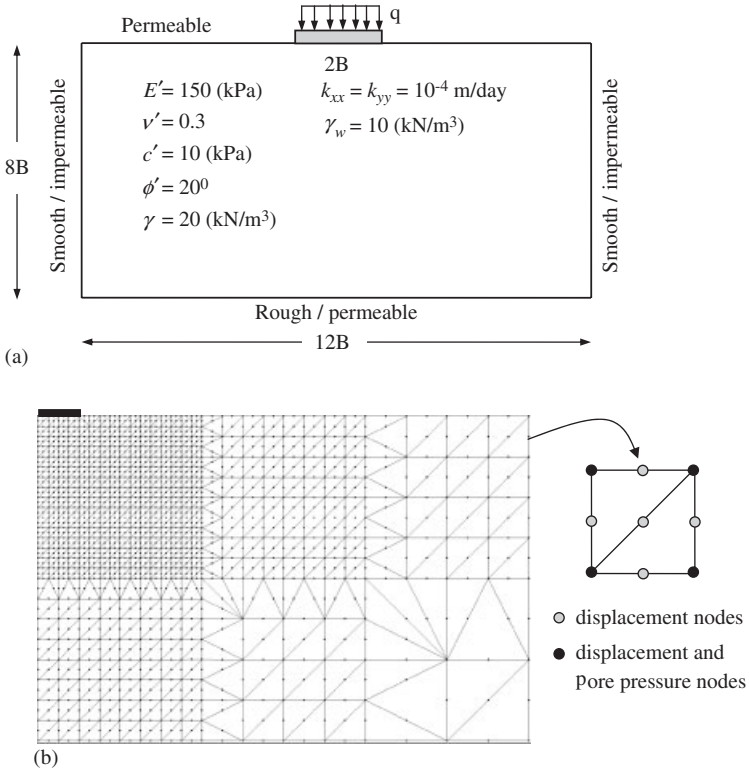

Figure 7. Rigid footing on an elastoplastic soil layer: (a) geometry, boundary conditions and material description and (b) finite element mesh of right-hand half of the footing, 872 elements and 1817 nodes.

is because of the coefficients of permeability which are kept constant in a small deformation analysis but they are a function of displacements in the ALE analysis. While the soil under the footing is deformed and consolidated, the permeability of the soil decreases. Therefore, the final settlement of the footing is achieved in a longer time compared with the analysis assuming constant coefficients of permeability. This example shows that the proposed ALE method is more efficient than the UL method in footing problems with large settlements. The deformed meshes for the small deformation analysis and the ALE analysis are shown in Figure 9. No mesh distortion can be observed in the ALE analysis.

4.3. Elastoplastic consolidation of a footing on a modified Cam–Clay material

In the third example, the performance of the UL and the ALE methods are compared in the case of modified Cam–Clay (MCC), a more complex soil model that is capable of simulating strain hardening and softening *via* one hardening parameter (the preconsolidation pressure). Again we study the consolidation settlement of a rigid footing, with the finite element mesh and material

DOI: 10.1002/nag

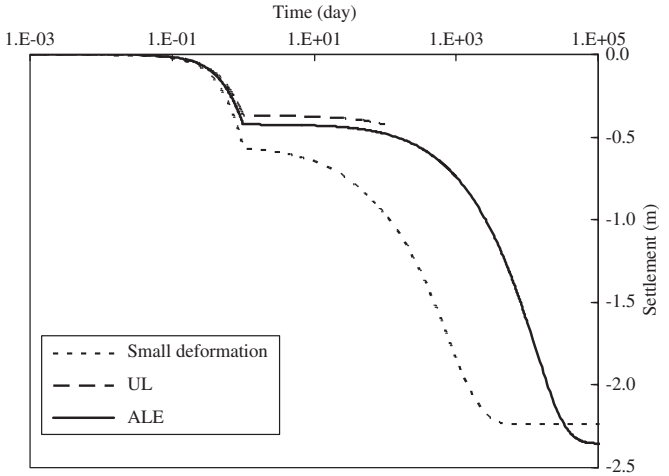

Figure 8. Settlement *versus* time for elastoplastic consolidation of the footing.

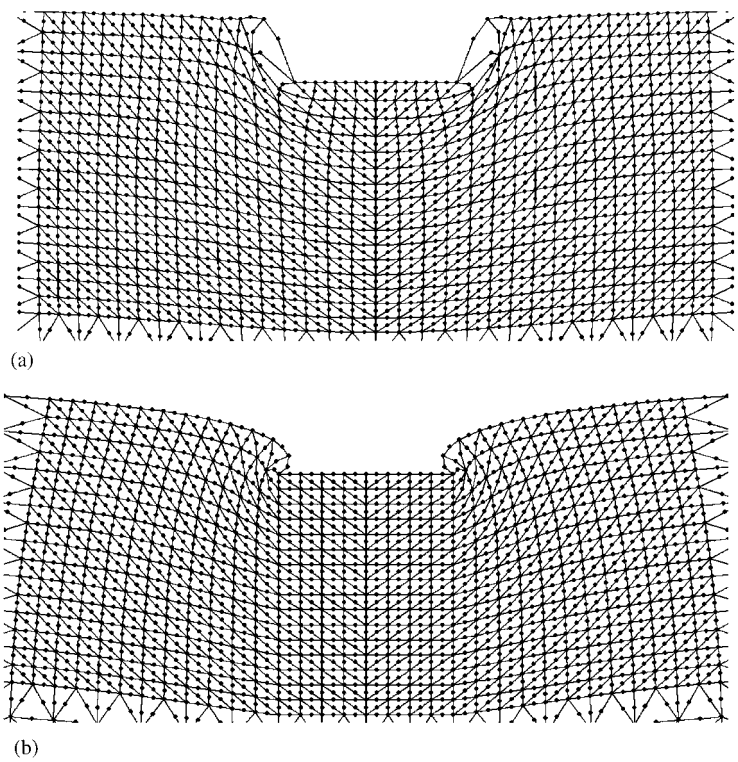

Figure 9. Deformation under footing on an elastoplastic soil: (a) small deformation, end of analysis and (b) the ALE method, end of analysis.

DOI: 10.1002/nag

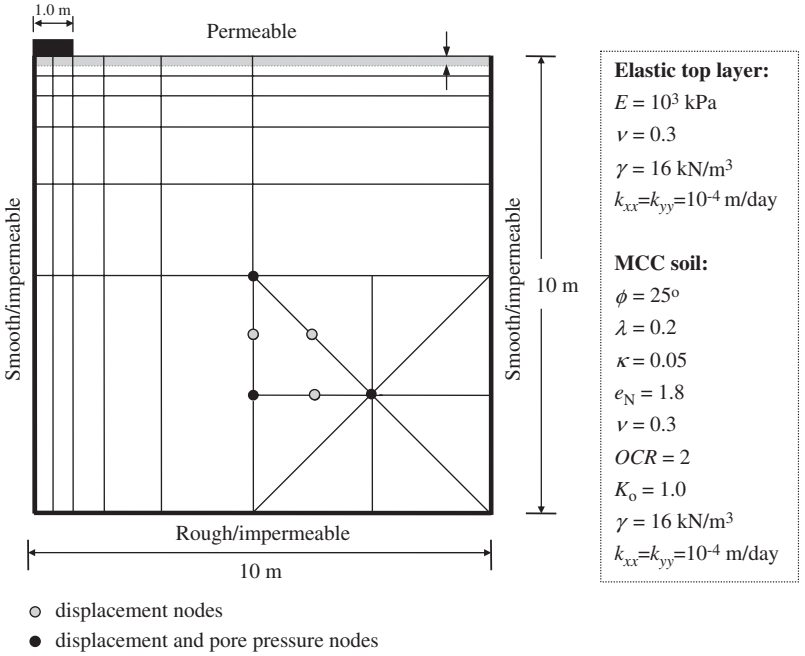

Figure 10. Finite element mesh for the consolidation of the rigid footing on an MCC soil (256 nodes, 288 elements).

properties shown in Figure 10. The parameters in Figure 10 include the following:

- λ: the slope of the normal compression line (NCL) in the space of the logarithmic mean stress $\ln p'$ *versus* the void ratio e,
- κ: the slope of the unloading-reloading line in the $\ln p' - e$ space,
- e_N: the intercept of the NCL on the e-axis when $\ln p\prime = 0$,
- OCR: the over-consolidation ratio of the soil,
- K_0: the coefficient of earth pressure at rest, and
- γ: the unit weight of the soil.

Note that the yield surface of the MCC model used in the analysis is a rounded Mohr–Coulomb hexagon in the deviatoric plane [36]. Because the MCC soil does not have any shear strength at zero mean stress, a thin layer of elastic material is added on top of the MCC soil to prevent a slope instability problem when the settlement of the footing becomes very large. Such a problem could also be avoided by introducing a small cohesion in the MCC model.

The analysis includes three stages. In the first stage, we use body force loading due to the self-weight of the soil to generate a non-zero initial stress field. The rate of this body force loading is set sufficiently small to establish a hydrostatic pore pressure profile in the soil. Once the initial stresses are established, the initial yield surface locations are determined according to the current stresses and the OCR. In the second stage, a uniform pressure q is applied on the footing over a period of 100 days. Two different values of $q = 40$ and 100 (kPa) are used for this step. Finally, the load q is kept constant and the soil is allowed to consolidate over time.

DOI: 10.1002/nag

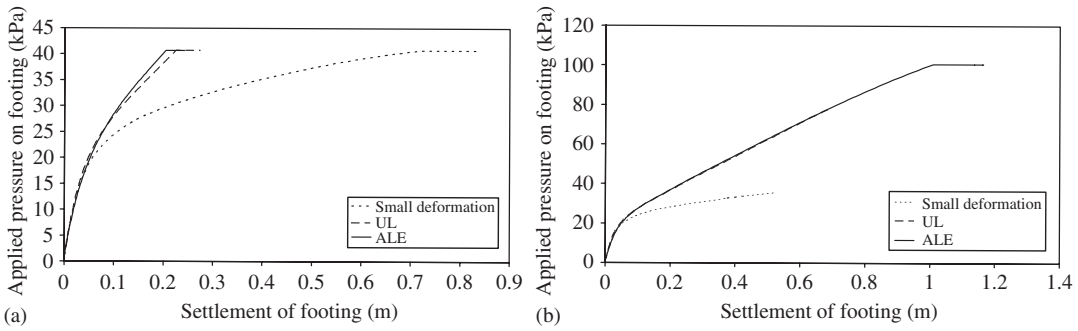

Figure 11. Settlement *versus* applied pressure on the footing: (a) $q = 40$ (kPa) and (b) $q = 100$ (kPa).

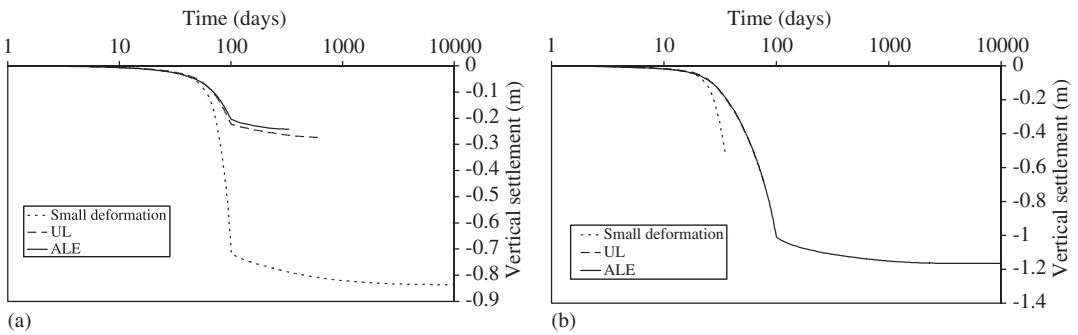

Figure 12. Settlement *versus* time for the footing on an MCC soil: (a) $q = 40$ (kPa) and (b) $q = 100$ (kPa).

Table I. Final settlement and the time for consolidation of footing on MCC soil.

Applied load (kPa)	Method	Final settlement (m)	Time (days)
$q = 40$	Small deformation	0.836	5100
	UL	0.274	630
	ALE	0.242	330
$q = 100$	Small deformation	0.528*	35
	UL	0.648*	77
	ALE (constant permeability)	1.165	3100

*Sudden termination of the analysis.

The predicted load–displacement curves are shown in Figure 11 and the settlement of the footing *versus* time is plotted in Figure 12. In both figures, we note there are significant differences between the large deformation results and the small deformation results. Table I summarizes the predicted final settlements of the footing and the corresponding times for each analysis. For $q = 40$ (kPa), the numerical results show that the difference between the UL method and the ALE method is not

DOI: 10.1002/nag

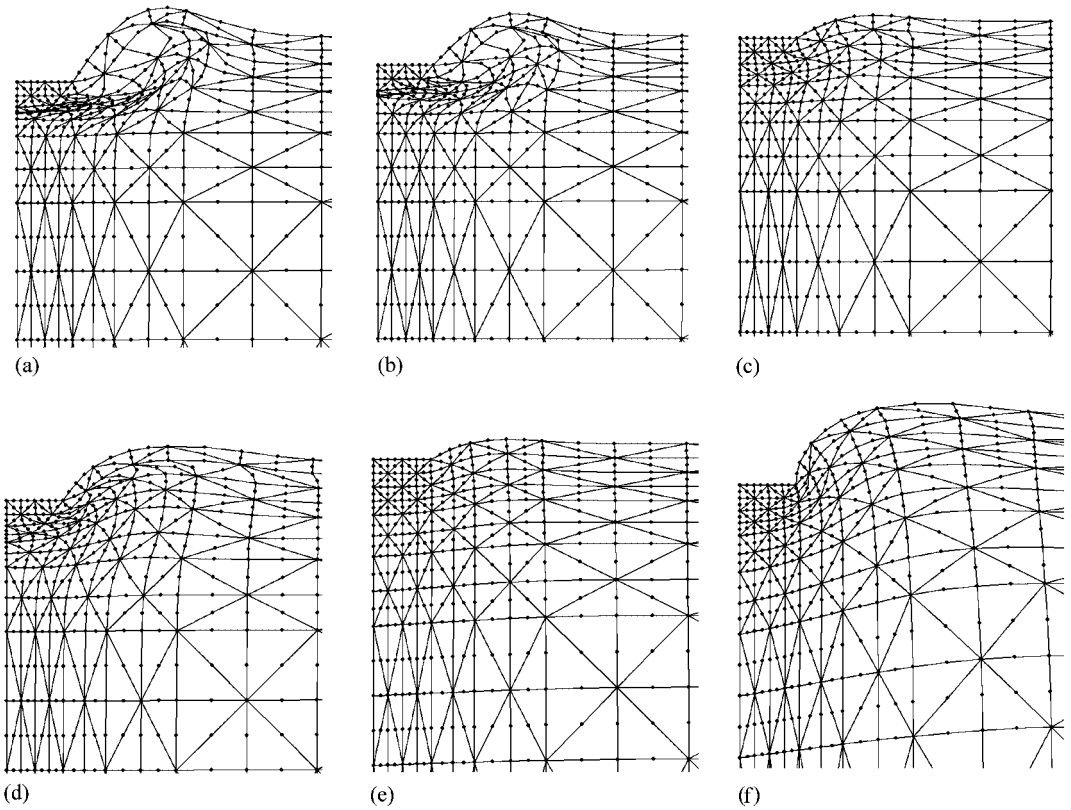

Figure 13. Deformed meshes under the footing from different methods: (a) small deformation, $q = 40$ (kPa), $t = 5100$ (days); (b) small deformation, $q = 100$ (kPa), $t = 35$ (days); (c) UL, $q = 40$ (kPa), $t = 630$ (days); (d) UL, $q = 100$ (kPa), $t = 77$ (days); (e) ALE, $q = 40$ (kPa), $t = 330$ (days); and (f) ALE, $q = 100$ (kPa), $t = 3100$ (days).

very significant since no mesh distortion occurs in this case. However, the difference between a small deformation and a large deformation analysis is noticeable. The final settlement of the footing predicted by small deformation analysis is 0.836 (m), which occurs after 5100 days (approximately 14 years). The final settlements predicted by the UL and ALE methods are 0.274 and 0.242 (m), respectively, occurring after 630 and 330 days (Figure 12(a)). In the case $q = 100$ (kPa), only the ALE method can complete the analysis and predict the final settlement of the footing. The small deformation analysis and the UL method stop spontaneously during the loading stage after 35 and 75 days, respectively. The former fails due to the applied load being larger than the small-strain collapse load while the latter fails because of mesh distortion. The total settlement of the footing predicted by the ALE method is found to be 1.165 (m) after 3100 days for this case (Figure 12(b)).

The deformed mesh for each analysis is shown in Figure 13. The meshes shown in Figure 13(b) and (d) are taken at the time just before the failure of the small deformation and the UL analyses, respectively. It can be seen that the deformed meshes for small deformation analyses are totally

DOI: 10.1002/nag

distorted. Some elements in the UL mesh for $q = 100\,\text{kPa}$ are also distorted at 77 days. However, the ALE meshes at the end of each analysis remain reasonably optimal (Figure 13(c)).

5. CONCLUSIONS

The Updated Lagrangian and arbitrary Lagrangian–Eulerian large deformation methods were generalized to handle coupled large deformation analysis of geomechanical problems in this paper. Some key conclusions drawn from this study are listed below.

1. Consolidation problems may involve large deformations for which the UL method cannot provide a solution. The ALE method based on the operator-split technique seems to provide an effective solution to such problems at finite strains.
2. The mesh refinement scheme adapted in this study works effectively and efficiently for the consolidation problems studied. The method is easy to implement into existing finite element codes and it does not require any complicated algorithms for mesh optimization.
3. Compared with single-phase materials involving only displacements, the main complications in the ALE treatment of consolidation problems are the convection of pore pressures and the update of the permeability. In this paper, the convection of the pore pressures is carried out at nodes instead of integration points. The permeability is treated as a function of the voids ratio.
4. In the ALE method based on the operator-split technique, the stresses, the hardening parameters and the pore pressures after the convection step usually violate global equilibrium and the local consistency condition since there is no objective remapping scheme for the state parameters. In this study, the consistency condition is satisfied by projecting the stress states back to the yield surface according to a drift correction scheme, which ensures that no strain is caused during the drift correction. Global equilibrium is achieved by additional Newton–Raphson iterations after the remapping of stresses. More research in this area is necessary.

APPENDIX A

The stiffness matrix, coupling matrix and vector of internal nodal forces in Equation (4) are given as follows:

$$[\mathbf{K^{ep}}] = \int_{V^t} [\mathbf{B}_L]^{\mathrm{T}} [\mathbf{C}'_{\mathrm{ep}}] [\mathbf{B}_L] \, \mathrm{d}V^t + \int_{V^t} [\mathbf{B}_{NL}]^{\mathrm{T}} [\boldsymbol{\sigma}'^t] [\mathbf{B}_{NL}] \, \mathrm{d}V^t + \int_{V^t} [\mathbf{B}_L]^{\mathrm{T}} [\overline{\boldsymbol{\sigma}}'^t] [\overline{\mathbf{B}}_L] \, \mathrm{d}V^t + \int_{V^t} [\mathbf{B}_{NL}]^{\mathrm{T}} [\mathbf{P}] [\mathbf{B}_{NL}] \, \mathrm{d}V^t \tag{A1}$$

$$[\mathbf{L}] = \int_{V^t} [\mathbf{B}_L]^{\mathrm{T}} \{\mathbf{m}\} [\mathbf{N}_p] \, \mathrm{d}V^t \tag{A2}$$

$$\{\mathbf{F}^{\mathrm{int}}\} = \int_{V^t} [\mathbf{B}_L]^{\mathrm{T}} \{\boldsymbol{\sigma}'\} \, \mathrm{d}V^t + \int_{V^t} [\mathbf{B}_L]^{\mathrm{T}} \{\mathbf{m}\} \{\mathbf{p}^t\} \, \mathrm{d}V^t \tag{A3}$$

DOI: 10.1002/nag

where for two-dimensional plane strain conditions, the corresponding **B** matrices at the ith node of an arbitrary element are defined as

$$[\mathbf{B}_L] = \begin{bmatrix} \dfrac{\partial N_i}{\partial x_1} & 0 & \dfrac{\partial N_i}{\partial x_2} \\ 0 & \dfrac{\partial N_i}{\partial x_2} & \dfrac{\partial N_i}{\partial x_1} \end{bmatrix}^{\mathrm{T}} \tag{A4}$$

$$[\mathbf{B}_{NL}] = \begin{bmatrix} \dfrac{\partial N_i}{\partial x_1} & \dfrac{\partial N_i}{\partial x_2} & 0 & 0 \\ 0 & 0 & \dfrac{\partial N_i}{\partial x_1} & \dfrac{\partial N_i}{\partial x_2} \end{bmatrix}^{\mathrm{T}} \tag{A5}$$

$$[\overline{\mathbf{B}}_L] = \begin{bmatrix} 0 & 0 & \dfrac{1}{2}\dfrac{\partial N_i}{\partial x_2} \\ 0 & 0 & -\dfrac{1}{2}\dfrac{\partial N_i}{\partial x_1} \end{bmatrix}^{\mathrm{T}} \tag{A6}$$

in which N denotes the nodal displacement shape functions.

For plane strain problems, the stress vectors and matrices in the above equations are

$$[\boldsymbol{\sigma}'^t] = \begin{bmatrix} \sigma'^t_{11} & \sigma'^t_{12} & 0 & 0 \\ \sigma'^t_{21} & \sigma'^t_{22} & 0 & 0 \\ 0 & 0 & \sigma'^t_{11} & \sigma'^t_{12} \\ 0 & 0 & \sigma'^t_{21} & \sigma'^t_{22} \end{bmatrix} \tag{A7}$$

$$[\overline{\boldsymbol{\sigma}}'^t] = \begin{bmatrix} 2\sigma'^t_{11} & 0 & 2\sigma'^t_{12} \\ 0 & 2\sigma'^t_{22} & -2\sigma'^t_{12} \\ \sigma'^t_{12} & \sigma'^t_{12} & \sigma'^t_{22} - \sigma'^t_{11} \end{bmatrix} \tag{A8}$$

$$[\mathbf{P}] = \begin{bmatrix} p & 0 & 0 & 0 \\ 0 & p & 0 & 0 \\ 0 & 0 & p & 0 \\ 0 & 0 & 0 & p \end{bmatrix} \tag{A9}$$

$$\{\boldsymbol{\sigma}'\} = \{\sigma'^t_{11} \quad \sigma'^t_{22} \quad \sigma'^t_{12}\}^{\mathrm{T}} \tag{A10}$$

$$\{\mathbf{p}^t\} = \{p^t_{11} \quad p^t_{22} \quad p^t_{12}\}^{\mathrm{T}} \tag{A11}$$

$$\{\mathbf{m}\} = \{1, 1, 0\}^{\mathrm{T}} \tag{A12}$$

DOI: 10.1002/nag

The flow matrix in Equation (7) is obtained from

$$[\dot{\mathbf{H}}] = \int_{V^t} \gamma_w^{-1} \cdot [\mathbf{B}_p]^{\mathrm{T}} [\mathbf{k}] [\mathbf{B}_p] \, \mathrm{d}V^t \tag{A13}$$

where $\mathbf{B}_p$ for plain strain problems is defined by

$$[\mathbf{B}_p] = \begin{bmatrix} \dfrac{\partial N_{p1}}{\partial x_1} & \dfrac{\partial N_{p2}}{\partial x_1} & \cdots & \dfrac{\partial N_{pm}}{\partial x_1} \\ \dfrac{\partial N_{p1}}{\partial x_2} & \dfrac{\partial N_{p2}}{\partial x_2} & \cdots & \dfrac{\partial N_{pm}}{\partial x_2} \end{bmatrix} \tag{A14}$$

and m is the number of nodes with pore pressure degree of freedom per element.

The fluid supply vector is calculated by

$$\{\dot{\mathbf{Q}}\} = -\int_{S^t} [\mathbf{N}_p]^{\mathrm{T}} q \, \mathrm{d}S^t - \int_{V^t} \gamma_w^{-1} \cdot [\mathbf{B}_p]^{\mathrm{T}} [\mathbf{k}] \{\mathbf{b}_w\} \, \mathrm{d}V^t \tag{A15}$$

REFERENCES

1. Biot MA. General theory of three-dimensional consolidation. *Journal of Applied Physics* 1941; **12**:155–169.
2. Carter JP, Small JC, Booker JR. A theory of finite elastic consolidation. *International Journal of Solids and Structures* 1977; **13**:467–478.
3. Carter JP, Booker JR, Small JC. The analysis of finite elasto-plastic consolidation. *International Journal for Numerical and Analytical Methods in Geomechanics* 1979; **3**:107–129.
4. Prevost JH. Mechanics of continuous porous media. *International Journal of Engineering Science* 1980; **18**: 787–800.
5. Prevost JH. Nonlinear transient phenomena in saturated porous media. *Computer Methods in Applied Mechanics and Engineering* 1982; **20**:3–18.
6. Zienkiewicz OC, Shiomi T. Dynamic behaviour of saturated porous media; the generalized Biot formulation and its numerical solution. *International Journal for Numerical and Analytical Methods in Geomechanics* 1984; **8**:71–96.
7. Meroi EA, Schrefler BA, Zienkiewicz OC. Large strain static and dynamic semisaturated soil behaviour. *International Journal for Numerical and Analytical Methods in Geomechanics* 1995; **19**:81–106.
8. Simo JC, Ortiz M. A unified approach to finite deformation elastoplastic analysis based on the use of hyperelastic constitutive laws. *Computer Methods in Applied Mechanics and Engineering* 1985; **49**:221–245.
9. Simo JC. A framework for finite strain elastoplasticity based on maximum plastic dissipation and the multiplicative decomposition: part I. Continuum formulation. *Computer Methods in Applied Mechanics and Engineering* 1988; **66**:199–219.
10. Simo JC. A framework for finite strain elastoplasticity based on maximum plastic dissipation and the multiplicative decomposition: part II. Computational aspects. *Computer Methods in Applied Mechanics and Engineering* 1988; **68**:1–31.
11. Borja RI, Alarcon E. A mathematical framework for finite strain elastoplastic consolidation. Part 1: balance laws, variational formulation, and linearization. *Computer Methods in Applied Mechanics and Engineering* 1995; **122**:145–171.
12. Borja RI, Tamagnini C, Alarcon E. Elastoplastic consolidation at finite strains. Part 2: finite element implementation and numerical examples. *Computer Methods in Applied Mechanics and Engineering* 1998; **159**:103–122.
13. Sanavia L, Schrefler BA, Steinmann P. A formulation for unsaturated porous medium undergoing large inelastic strains. *Computational Mechanics* 2002; **28**(2):137–151.
14. Nazem M, Sheng D, Carter JP. Stress integration and mesh refinement in numerical solutions to large deformations in geomechanics. *International Journal for Numerical Methods in Engineering* 2006; **65**:1002–1027.
15. Benson DJ. An efficient, accurate and simple ALE method for nonlinear finite element programs. *Computer Methods in Applied Mechanics and Engineering* 1989; **72**:305–350.

DOI: 10.1002/nag

16. Bathe KJ. *Finite Element Procedures*. Prentice-Hall: Englewood Cliffs, NJ, 1996.
17. Potts DM, Zdravkovic L. *Finite Element Analysis in Geotechnical Engineering*. vol. 1. Thomas Telford Publishers: England, 2001.
18. Booker JR, Small JC. An investigation of the stability of numerical solutions of Biot's equations of consolidation. *International Journal of Solids and Structures* 1975; **11**:907–917.
19. Wood WL. *Practical Time-stepping Schemes*. Clarendon Press: Oxford, 1990.
20. Lewis RW, Schrefler BA. *Finite Element Method in Static and Dynamic Deformation and Consolidation of Porous Media* (2nd edn). Wiley: Chichester, U.K., 1998.
21. Sloan SW, Abbo AJ. Biot consolidation analysis with automatic time stepping and error control. Part 1: theory and implementation. *International Journal for Numerical and Analytical Methods in Geomechanics* 1999; **23**:467–492.
22. Sheng D, Sloan SW. Time stepping schemes for coupled displacement and pore pressure analysis. *Computational Mechanics* 2003; **31**:122–134.
23. Hughes TJR, Winget J. Finite rotation effects in numerical integration of rate constitutive equations arising in large-deformation analysis. *International Journal for Numerical Methods in Engineering* 1980; **15**:1862–1867.
24. Sloan SW, Abbo AJ, Sheng D. Refined explicit integration of elastoplastic models with automatic error control. *Engineering Computations* 2001; **18**:121–154. (Erratum: *Engineering Computations* 2002; **19**(5/6):594–594.)
25. Lambe TW, Whitman RV. *Soil Mechanics*. Wiley: New York, 1979.
26. Das BM. *Principles of Geotechnical Engineering*. PWS Publishing Company: Boston, MA, 1994.
27. Nazem M, Sheng D. Alternative solution methods for large deformations in geomechanics. *Proceedings of the 9th Symposium on Numerical Models in Geomechanics-NUMOG IX*, Ottawa, Canada, 2004; 265–271.
28. Hughes TJR, Liu WK, Zimmermann TK. Lagrangian–Eulerian finite element formulation for incompressible viscous flow. *Computer Methods in Applied Mechanics and Engineering* 1981; **58**:19–36.
29. Lopez RJ. *Advanced Engineering Mathematics*. Addison-Wesley: New York, 2001.
30. Zienkiewicz OC, Zhu JZ. The superconvergent patch recovery and a posteriori error estimates. Part 1: the recovery technique. *International Journal for Numerical Methods in Engineering* 1992; **33**:1331–1364.
31. Zienkiewicz OC, Chan AHC, Pastor M, Schrefler BA, Shiomi T. *Computational Geomechanics with Special Reference to Earthquake Engineering*. Wiley: Chichester, England, 1999.
32. Burd HJ. A large displacement finite element analysis of a reinforced unpaved road. *Ph.D. Thesis*, Oxford University, England, 1986.
33. Small JC. Elasto-plastic consolidation of soils. *Ph.D. Thesis*, University of Sydney, Australia, 1977.
34. Yu HS. *Cavity Expansion Methods in Geomechanics*. Kluwer Academic Publishers: The Netherlands, 2000.
35. Yu HS. Cavity expansion theory and its application to the analysis of pressuremeters. *Ph.D. Thesis*, Oxford University, England, 1990.
36. Sheng D, Sloan SW. Load stepping methods for critical state models. *International Journal for Numerical Methods in Engineering* 2001; **50**(1):67–93.

DOI: 10.1002/nag